Cell Reports
Medicine

Article

# Space-time-regulated imaging analyzer for smart coagulation diagnosis

## Graphical abstract

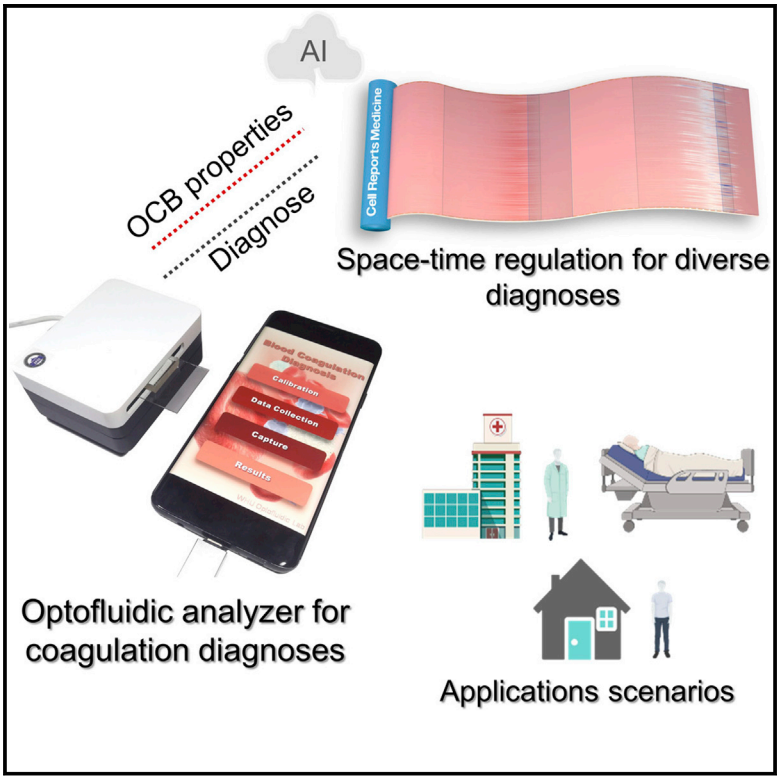


## Authors

Longfei Chen, Le Yu, Yantong Liu, ..., Long Bai, Fubing Wang, Yimin Zhu

## Correspondence

yangyiys@whu.edu.cn

## In brief

Chen et al. report a method for coagulation function diagnoses using intelligent optical clotting biophysics (OCB) properties identification. The developed space-time regulation of OCB properties allows diverse diagnoses and contributes to potential diagnostic-markers exploration. It possesses good portability and should empower low-cost and convenient diagnoses in extensive clinical scenarios.

## Highlights

- An ultraportable optofluidic analyzer empowers convenient coagulation diagnoses
- The system enables optical clotting biophysics (OCB) properties acquisition and process
- Coagulation function diagnoses uses intelligent OCB properties identification
- Space-time regulation of OCB properties endow it capability to diverse diagnoses

Chen et al., 2022, Cell Reports Medicine *3*, 100765
October 18, 2022 
https://doi.org/10.1016/j.xcrm.2022.100765

CellPress

Cell Reports Medicine

CellPress
OPEN ACCESS

Article

# Space-time-regulated imaging analyzer for smart coagulation diagnosis

Longfei Chen,[1,2,3,7] Le Yu,[1,2,3,7] Yantong Liu,[1,2,3,7] Hongshan Xu,[1] Linlu Ma,[4] Pengfu Tian,[1] Jiaomeng Zhu,[1] Fang Wang,[1] Kezhen Yi,[5] Hui Xiao,[4] Fuling Zhou,[4] Yi Yang,[1,2,3,8,*] Yanxiang Cheng,[2] Long Bai,[6] Fubing Wang,[5] and Yimin Zhu[6]

[1]Key Laboratory of Artificial Micro- and Nano- Structures of Ministry of Education, School of Physics & Technology, Wuhan University, Wuhan 430072, China
[2]Renmin Hospital, Wuhan University, Wuhan 430060, China
[3]Shenzhen Research Institute, Wuhan University, Shenzhen 518000, China
[4]Department of Hematology, Zhongnan Hospital, Wuhan University, Wuhan 430071, China
[5]Department of Laboratory Medicine, Zhongnan Hospital, Wuhan University, Wuhan 430071, China
[6]School of Medicine, Zhejiang University, Hangzhou, Zhejiang 310002, China
[7]These authors contributed equally
[8]Lead contact
*Correspondence: yangyiys@whu.edu.cn
https://doi.org/10.1016/j.xcrm.2022.100765

## SUMMARY

The development of intelligent blood coagulation diagnoses is awaited to meet the current need for large clinical time-sensitive caseloads due to its efficient and automated diagnoses. Herein, a method is reported and validated to realize it through artificial intelligence (AI)-assisted optical clotting biophysics (OCB) properties identification. The image differential calculation is used for precise acquisition of OCB properties with elimination of initial differences, and the strategy of space-time regulation allows on-demand space time OCB properties identification and enables diverse blood function diagnoses. The integrated applications of smartphones and cloud computing offer a user-friendly automated analysis for accurate and convenient diagnoses. The prospective assays of clinical cases (n = 41) show that the system realizes 97.6%, 95.1%, and 100% accuracy for coagulation factors, fibrinogen function, and comprehensive blood coagulation diagnoses, respectively. This method should enable more low-cost and convenient diagnoses and provide a path for potential diagnostic-markers finding.

## INTRODUCTION

Assessment of the blood coagulation function is crucial in many time-sensitive clinical settings, including surgery, transfusion, trauma etc., to predict, avoid, and guide the management of serious diseases caused by bleeding or thrombosis.[1–4] Current clinical monitoring methods mainly rely on active stimulus-response systems (monitoring probes, resonance, etc.). These active stimulus-response methods often require precise input source-detector modules. This leads to the complexity of current equipment, and the well-trained operation needed, for example, a widely used clinical thromboelastography analyzer, the TEG (TEG5000, Denver, CO, USA) performs thromboelastography detection by monitoring the amplitude changes of a high-precision probe.[5–8] In addition, active stimulation methods (probes, particle motion, resonance) will affect the stability of the clot; clot fragmentation and dislodgement often occur in practical clinical applications, thus interfering with the measurement. The disruptive technology development for blood coagulation function diagnosis is urgently needed and widely expected.

Currently, a series of good studies about optofluidic imaging systems combined artificial intelligence (AI) for smart disease diagnosing are gradually emerging,[8–24] which implies a potential possibility of combining optical imaging and AI technologies for convenient and accurate smart blood coagulation function diagnoses. Blood clotting is a continuous process that includes clotting activation, formation, and densification, and the patients differ in the rate and intensity of each process.[25–27] Therefore, AI-assisted single clotting image recognition has trouble accurately assessing the comprehensive blood coagulation capacity. In addition, the clinical diseases induce changes in the oxygen content of the blood red cells, which leads to inconsistent initial chromaticity and optical intensity of the clotting images, and it further interferes with the accuracy of AI-assisted coagulation imaging recognition.[28,29] The real clinical application of this promising method is still a challenge.

Here, we propose a convenient and scalable approach to realize it, based on AI-assisted space-time regulation of optical clotting biophysics (OCB) properties (Figure 1). The developed optical imaging system[9,30–32] enables continuous clotting imaging capture, and the images' differential calculation was used to precisely acquire the OCB properties with elimination of initial differences.[10] Space-time regulation of OCB properties is used to enable diverse coagulation function diagnoses. Simply, the different coagulation function diagnoses were realized by OCB properties segmentation and combination. The regulated OCB

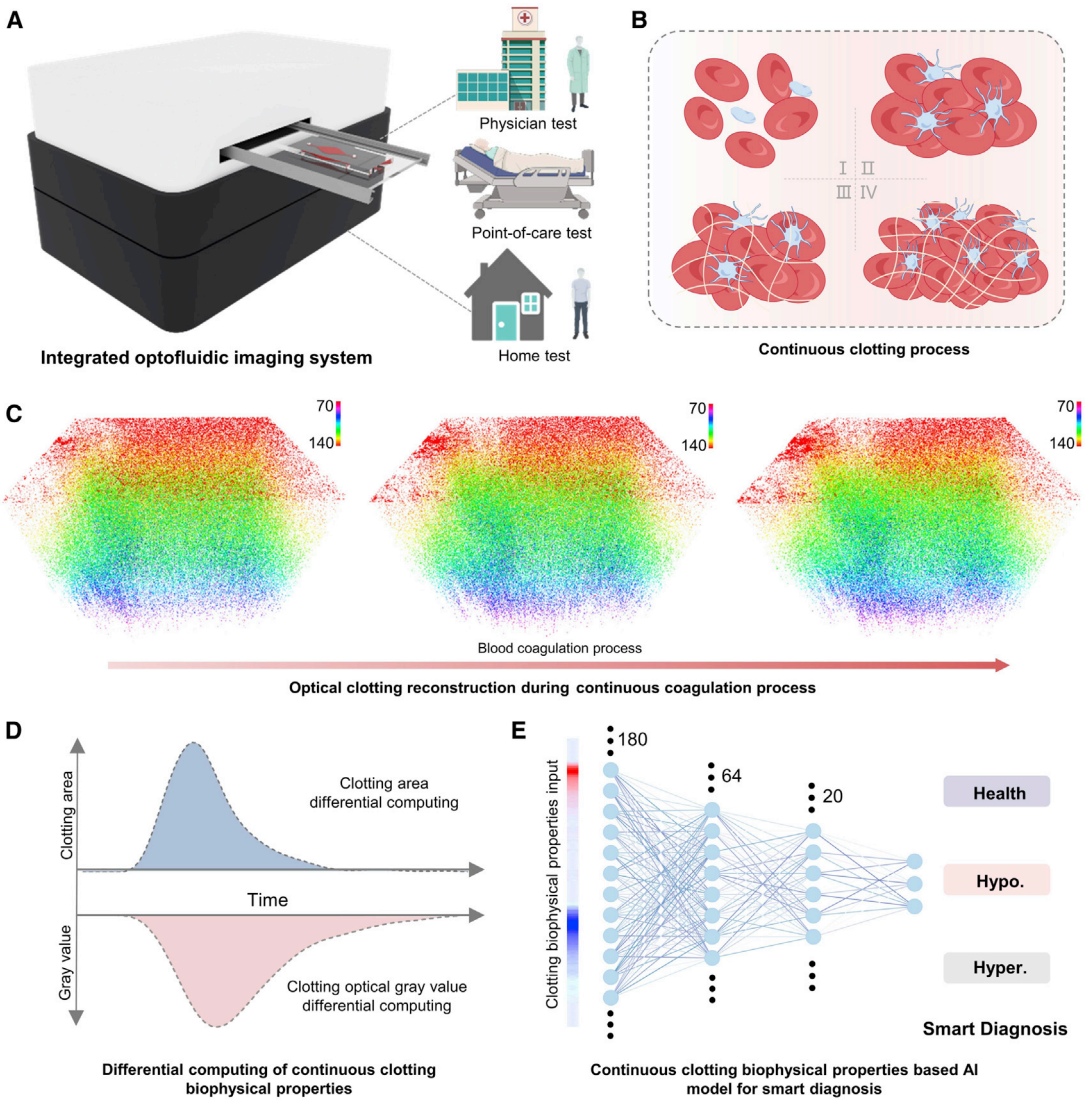


**Figure 1. Working principle and application scenarios of this system**

(A) The developed system and promising applications.

(B) The schematic diagram of the continuous clotting process. (I) Pre-clotting, (II) activated clotting, (III) clotting growth, and (IV) clotting densification.

(C) The optical clotting reconstruction of the clotting during continuous coagulation process. The color bar refers to the gray value.

(D) The collected continuous optical clotting biophysical (OCB) properties with differential computing.

(E) The OCB properties-based deep-learning model for smart blood coagulation diagnosis.

properties were then imported to neural networks for accurate and automated diagnoses. We then prospectively tested the method in human subjects for usability and accuracy against a standard clinical device. Our results support clinical equivalency in accuracy. This method should meet large-scale and time-sensitive clinical caseload need.

## RESULTS

### On-chip blood clotting process

After blood injection, the good seal of the chip was realized by oil sealing[20] (Figure S2). The fluorescent characterization was then performed to clearly and dynamically display the on-chip blood clotting process. The confocal micrographs of the continuous clotting process for platelet (PLT) bound to fibrin (FIB) are shown in Figure 2A, and the three-dimensional fluorescence intensity maps are shown in Figure 2B. The results (Figures 2C and 2D) show that the 5, 15, 25, and 35 min average PLT fluorescent areas were 0.485 ($\sigma$ = 0.033), 0.507 ($\sigma$ = 0.042), 0.612 ($\sigma$ = 0.051), and 0.654 ($\sigma$ = 0.054), respectively. The average FIB fluorescent areas were 0.083 ($\sigma$ = 0.013), 0.146 ($\sigma$ = 0.024), 0.231 ($\sigma$ = 0.031), and 0.250 ($\sigma$ = 0.035), respectively. This shows the growth of the on-chip blood clot. The 5, 15, 25, and 35 min average PLT fluorescence intensities were 149.916 ($\sigma$ = 2.780),

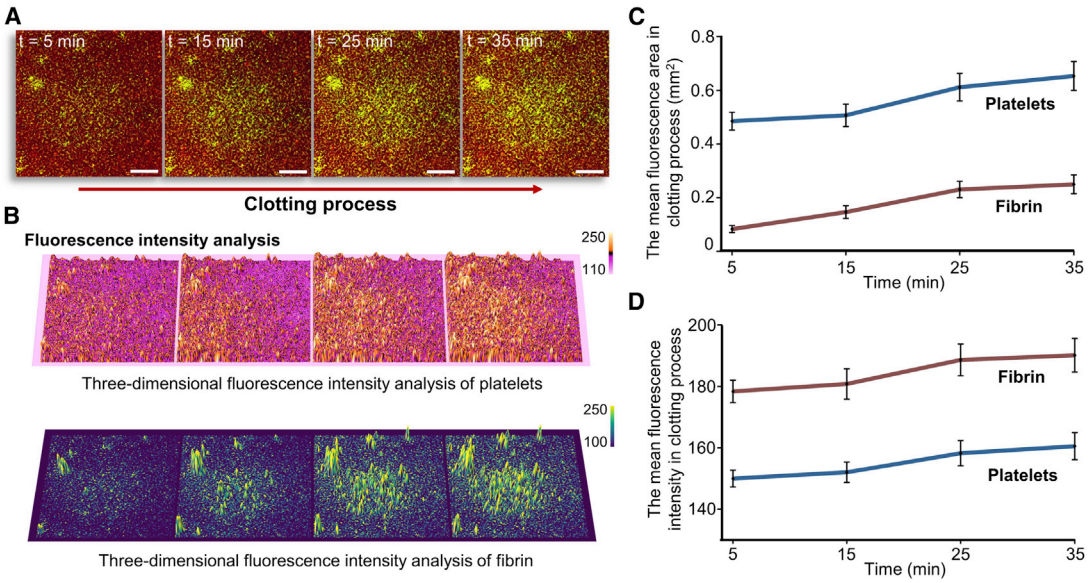


**Figure 2. On-chip clotting process**

(A) The confocal micrographs of continuous clotting process for platelet (red) bound to fibrin (green). Scale bar: 200 μm.

(B) The three-dimensional fluorescence intensity maps of platelets and fibrin.

(C) The mean fluorescence area of platelets and fibrin during blood clotting process (n = 5). The error bars refer to standard deviation.

(D) The mean fluorescence intensity of platelets and fibrin during blood clotting process (n = 5). The error bars refer to standard deviation.

152.033 ($\sigma$ = 3.360), 158.249 ($\sigma$ = 4.120), and 160.547 ($\sigma$ = 4.456), respectively, and the corresponding average FIB fluorescence intensities were 178.371 ($\sigma$ = 3.694), 180.843 ($\sigma$ = 4.973), 188.606 ($\sigma$ = 5.213), and 190.151 ($\sigma$ = 5.491), respectively. This indicates the increased clot intensity in the chip. Overall, these on-chip results indicate that blood clotting is a continuous process—the FIB gradually forms and webs the blood cells to form clotting—and the increase in FIB fluorescence area indicates the clotting growth process, while the increase in the average PLT fluorescence intensity demonstrates the increased clotting compactness.[18,33,34] And, it inspired us to perform source-free monitoring of the clotting process by the continuous biophysical properties changes (clotting growth and densification).

## OCB properties acquisition and processing

The continuous process of blood clotting includes the activation of the coagulation process, where thrombin is then released to activate fibrinogen to form FIB, and it webs the blood cells to form blood clotting.[18,35–39] This in turn leads to regular changes in optical clotting properties. Through the designed optical imaging system (field of view [H × V, mm]: 1.81 × 1.02, resolution: 1 μm; Figure S1),[9] the smartphone enables continuous images capture in the blood clotting process. Figure 3A shows the operational interface of the smartphone data acquisition (continuous clotting process capture) and the analysis process. In the clotting growth and densification process, the optical intensity (gray value) of blood clotting changes accordingly. As in the clotting growth process, the blood clotting area with decreased gray value will expand, and in the densification process, the optical gray value of the clotting area will further decrease.[18,35] Therefore, the quantification of clotting area and compactness can be achieved by identifying the gray value changes of the clotting images, and the optical reconstructed treatment process (Video S1) has been shown in Figure 3B. Figure 3C shows the recorded continuous OCB properties (clotting area and optical gray value) from a patient based on this system. Differential computing was used to eliminate the interference of the differences in initial blood gray value (Figure S3) on the quantification of the OCB properties,[40,41] and the OCB properties' curves with differential computing process are shown in Figure 3D. In this blood sample, the initial flat straight line refers to the pre-clotting state. After entering the clotting state, the curve of the blood clotting area significantly increases (clotting growth), and the curve of the average clotting optical gray value decreases (clotting densification). The clotting then reaches a steady state (insignificant changes in clotting area and average optical gray value).[18]

## Intelligent blood coagulation diagnosis

In this study, 163 clinical patient blood samples were collected and analyzed (room temperature: 26°C) for space-time-regulated diagnoses model development, and Figure 4A presents the differences in OCB properties of the 163 clinical patients between hypercoagulable, normal, and hypocoagulable patients (90 healthy; 42 hypocoagulation; 31 hypercoagulation). The 3D t-distributed stochastic neighbor embedding (T-SNE) plots are shown in Figure 4B. It is clear to see that this method has good discrimination for different comprehensive coagulation, and it is distinct in phenotypic space visualized by T-SNE. We performed AI diagnoses model development for

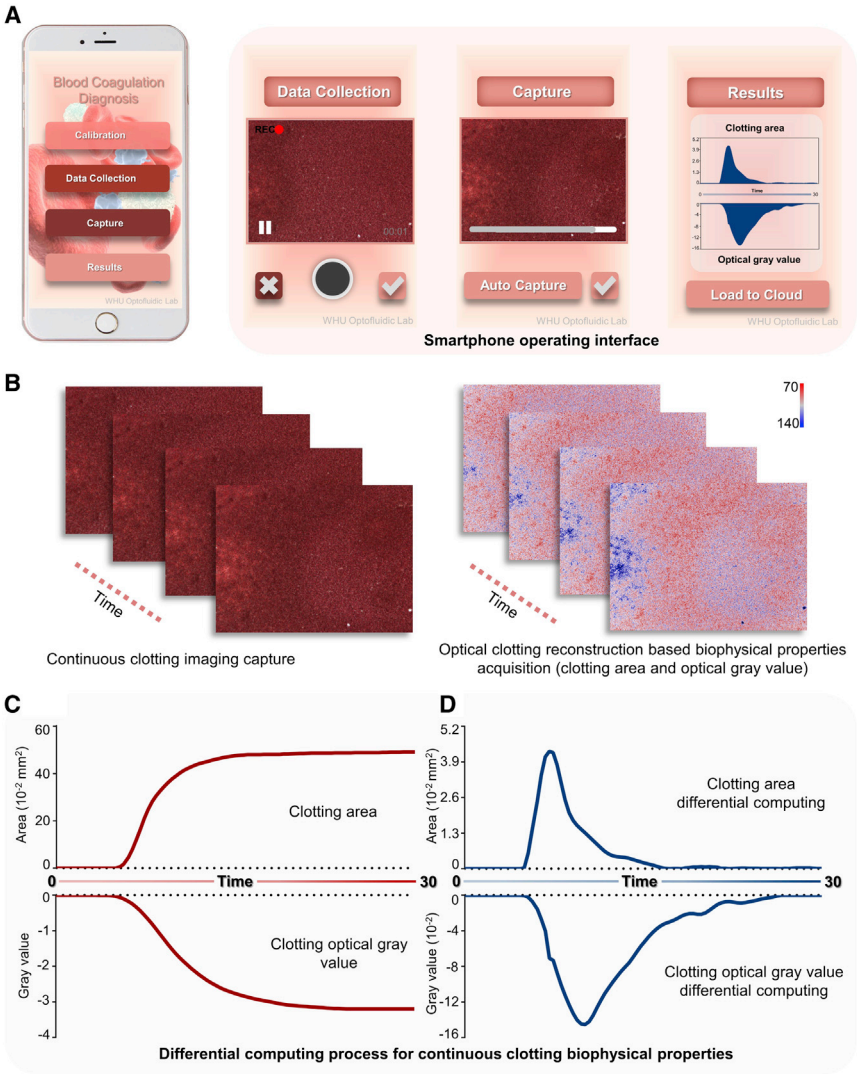


**Figure 3. Edge computing-based OCB properties acquisition and processing**

(A) The operational interface of the smartphone for data acquisition and analysis.

(B) The image's treatment process for OCB properties acquisition.

(C and D) Differential computing process of continuous OCB properties.

comprehensive coagulation diagnosis (Figure 4C), and the model possesses a good accuracy of 98.6% (space-time interval: 0–30 min).

We then performed space-time regulation for smart fibrinogen function and coagulation factor diagnoses. As shown in Figure S6A, the AI models for fibrinogen function diagnosis (97 normal type; 48 low type; 18 exceeded type) with space-time regulation (5–15, 5–20, 5–25 min) were performed, and the results show that the deep-learning model based on the 5–20 min regulation interval has a best test accuracy of 96.0% (94.5% diagnosing accuracy of normal type, 98.9% diagnosing accuracy of low type, 96% diagnosing accuracy of exceeded type); the AI model based on the 5–15 min regulation interval has a test accuracy of 95.2% (95.9% diagnosing accuracy of normal type, 92.8% diagnosing accuracy of low type, 100% diagnosing accuracy of exceeded type); and the AI model based on the 5–25 min regulation interval has a test accuracy of 94.8% (92.7% diagnosing accuracy of normal type, 97.5% diagnosing accuracy of low type, 99% diagnosing accuracy of exceeded type). Therefore, the 5–20 regulation interval was selected for fibrinogen function diagnose, and the heatmap of space-time-regulated OCB properties is shown in Figure 4D. As shown in Figure S6B, the AI models for coagulation factor diagnosis (91 normal type; 42 low type; 30 exceeded type) with space-time regulation (0–5, 0–8, 0–11 min) were performed. The results show that the deep-learning model based on the 0–8 min regulation interval has a best test accuracy of 96.1% (97.2% diagnosing accuracy of normal type, 100% diagnosing accuracy of low type, 86.2% diagnosing accuracy of exceeded type); the AI model based on the 0–5 min regulation interval has a test accuracy of 91.9% (91.9% diagnosing accuracy of normal type, 96.7% diagnosing accuracy of low type, 85% diagnosing accuracy of exceeded type); and the AI model based on the 0–11 min regulation interval has a test accuracy of 95.1% (97.6% diagnosing accuracy of normal type, 98.3% diagnosing accuracy of low type, 81.9% diagnosing accuracy of exceeded type). Therefore, the 0–8 regulation interval was selected due to the best accuracy. The 3D T-SNE plots are shown in Figure 5A, and it is clearly distinguished in phenotypic space visualized by T-SNE, and the heatmap (Figure 5B) presents the differences in 0–8 min OCB properties between different types.

## Clinical assays

Following AI model development, we proceeded to patient-oriented testing for clinical comprehensive blood coagulation, fibrinogen, and coagulation factor function diagnoses. A prospective trial with 41 patients in Zhongnan Hospital was designed for double-blind test against a clinical standard instrument. All patients gave informed consent for the extra test. Figure 6C shows a histogram of the comprehensive blood coagulation distribution in 41 patients based on physicians' diagnoses including health, hypocoagulation, and hypercoagulation, and the confusion matrix for comparison of physician annotation diagnosing with this method is shown in Figure 6D. The results show 100% accuracy of comprehensive blood coagulation diagnosis with this method. Figure 6E shows a histogram of the fibrinogen function distribution in 41 patients based on physicians' diagnoses, which includes normal, low, and exceeded types, and

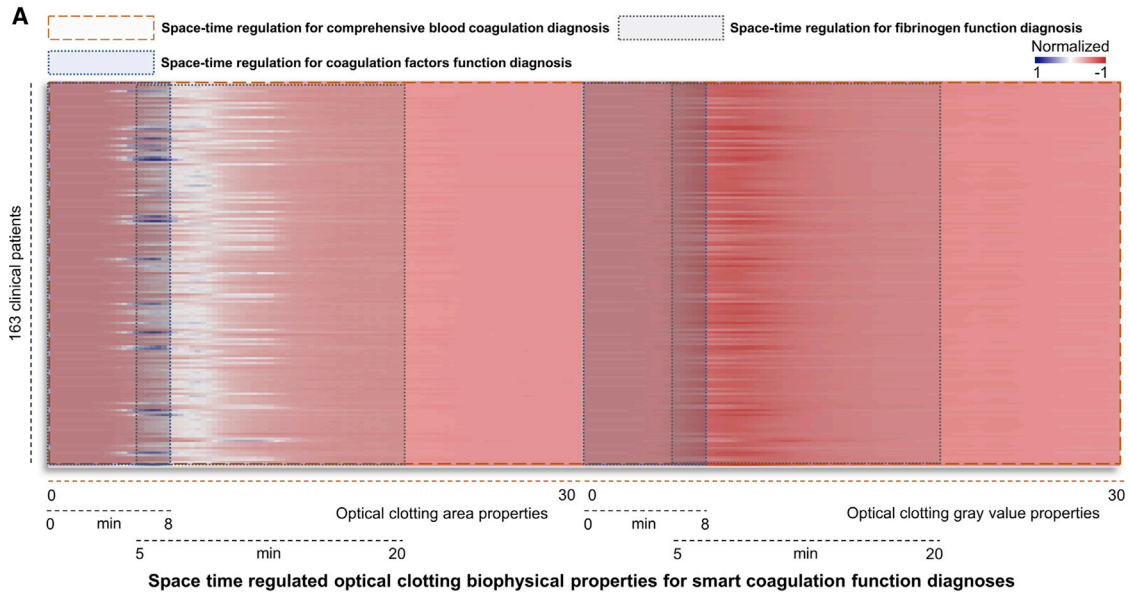


Space time regulated optical clotting biophysical properties for smart coagulation function diagnoses

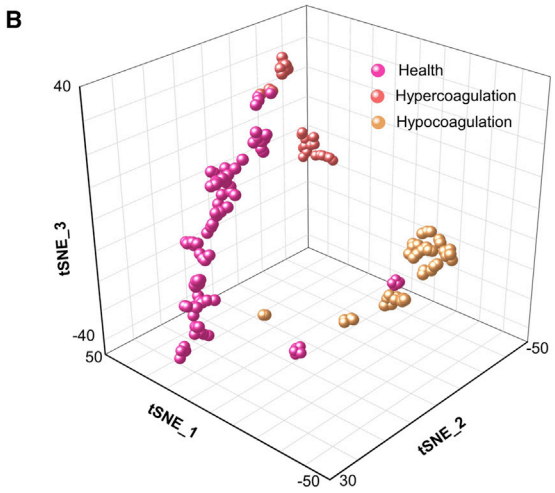


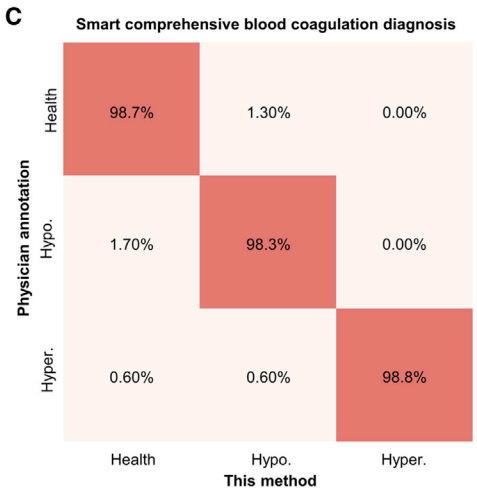


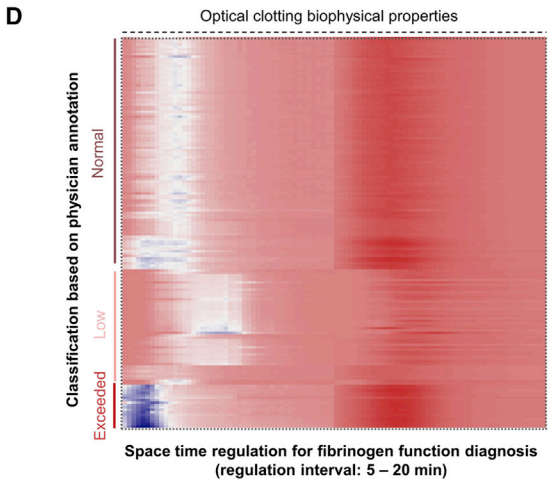


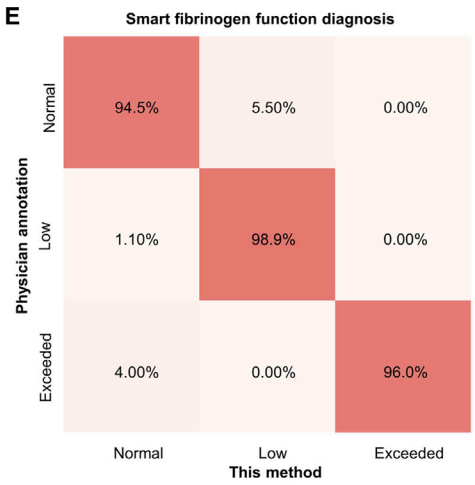


*(legend on next page)*

the confusion matrix for comparison of physician annotation diagnosing with this method is shown in Figure 6F. The results show that this method realizes 95.1% accuracy of fibrinogen function diagnosis with this method. Figure 7A shows a histogram of the coagulation factor distribution (normal, low, and exceeded types) in 41 patients based on physicians' diagnoses, and the confusion matrix for comparison of physician annotation diagnosing with this method is shown in Figure 7B. The results show that this method realizes 97.6% accuracy of coagulation factor diagnosis with this method. Overall, this method supports clinical equivalency in diagnostical accuracy compared with standard physician annotation diagnosing. These results also validate the feasibility and scalability of this method.

## DISCUSSION

Here, a brand-new method was proposed and validated to enable convenient and accurate coagulation function diagnoses via AI-assisted space-time regulation of OCB properties. The developed optical imaging system enables continuous and accurate space-time-based OCB properties acquisition, while image differential computing was used to eliminate the interference of initial patients' clotting optical intensity differences, and the diverse coagulation function diagnoses were realized through space-time regulation of OCB properties. The feasibility and performance of the method have been validated by prospective clinical assays in which it exhibits a 97.6% accuracy for coagulation factors, a 95.1% accuracy for fibrinogen function, and 100% accuracy for comprehensive blood coagulation.

Some good works have been reported for clinical optical coagulation diagnoses, which mainly rely on a light-scattering basis.[42,43–45] But the multiple scattering interference of the clotting and high equipment requirement make it hard to balance portability and clinical accuracy. For example, Guzman Sepulveda et al. have performed a good study about a precise and specialized optical fiber system for blood coagulability monitoring.[42] While in microscopic coagulation monitoring (microfluidic system), there is no significant light-scattering interference due to the large specific surface area of blood,[2,18,36] this gives a good platform for combined intelligent coagulation diagnosis. However, blood clotting is a continuous process, and there are differences in the initial optical intensity of patients' blood samples due to diseases. Therefore, AI-assisted single clotting image recognition has trouble meeting the accurate clinical coagulation function diagnosis needed; it is also the reason that current clinical and state-of-art smart devices for blood coagulation diagnosis mainly rely on mechanical properties monitoring of the clotting (active-sources methods: physical vibration, particle motion, etc.).[46,47] In this work, we explore and validate a method using space-time-regulation-assisted intelligent OCB properties identification for intelligent coagulation function diagnoses, which characterizes low-cost, smart, and automated diagnoses. This method also has excellent portability and compatibility with smartphones, mobile Raspberry Pi (RPi), computers, clouds, etc., which should enable extensive clinical application scenarios. We have currently implemented the integrated applications of smartphone and cloud technologies, which should empower low-cost and convenient clinical coagulation function diagnoses in many clinical settings (hospitals, community medical centers, homes, etc.) and contribute to new diagnostic markers finding.

### Limitations of the study

The main limitation of our study is the relatively small sample size of the clinical patients we examined. The clinical patient engagement, diversity, and breadth are not sufficient to support more coagulation function diagnosis model development and new diagnostic markers finding. For example, we were unable to develop the model for fibrinolytic function diagnosis due to the absence of significant fibrinolysis in the volunteered clinical patients. We would incorporate more disease characterization factors to further enrich it in the future. The main limitation of our device is the current inability to incorporate flow fields, endothelial function, etc. into the system for personalized diagnostic needs. Benefiting from the high scalability of microfluidic systems, it may be realized with the further development of microfluidic pumpless directional infusion technology and organ-on-a-chip technology.[48,49] In addition, this system is aimed and designed to meet the need for convenient, low-cost testing and tremendous clinical applications; therefore, we did not use an additional external temperature control module and pump modules but used room temperature measurement and blood perfusion to achieve the lightness and low cost of the device (<$100). In light of the potential applications in low-resource areas, this method can also run on the Raspberry Pi platform in low-resource areas without a network connection.[50]

## STAR★METHODS

Detailed methods are provided in the online version of this paper and include the following:

- KEY RESOURCES TABLE
- RESOURCE AVAILABILITY
  - Lead contact
  - Materials availability
  - Data and code availability
- EXPERIMENTAL MODEL AND SUBJECT DETAILS
- METHOD DETAILS
  - Fabrication of the optofluidic chip

**Figure 4. Space-time regulation for smart comprehensive coagulation and fibrinogen function diagnoses**

(A) The vector's heatmap of the OCB properties, and space-time regulation for smart comprehensive coagulation, fibrinogen, and coagulation factor function diagnosis.

(B) Three-dimensional T-SNE map of OCB properties for smart comprehensive coagulation diagnosis (regulation interval: 0–30 min).

(C) Confusion matrices comparing the performance for comprehensive coagulation diagnosis between expert diagnosis and this method.

(D) The vector's heatmap of the OCB properties for fibrinogen function diagnosis (regulation interval: 5–20 min).

(E) Confusion matrices comparing the performance for smart fibrinogen function diagnosis between expert diagnosis and this method.

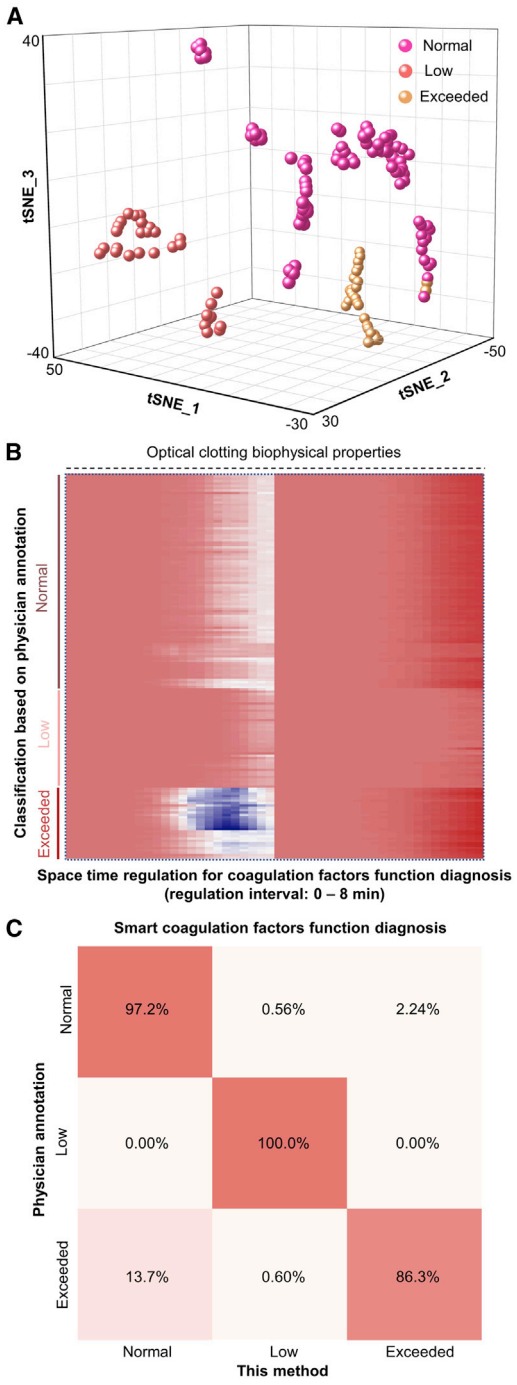


**Figure 5. Space-time regulation for smart coagulation factor function diagnose**

(A) Three-dimensional T-SNE map of OCB properties for smart coagulation factor function diagnosis (regulation interval: 0–8 min).

(B) The vector's heatmap of the OCB properties for coagulation factor function diagnosis (regulation interval: 0–8 min).

(C) Confusion matrices comparing the performance for smart coagulation factors function diagnosis between expert diagnosis and this method.

- Design of the portable imaging system
- Image differential computing process for clotting biophysical properties acquisition
- Developed deep learning system
- Image acquisition interval selection
- Fluorescence characterization of clotting
- Blood assays
- Comparison of third-party TEG instrument test

- QUANTIFICATION AND STATISTICAL ANALYSIS

## SUPPLEMENTAL INFORMATION

Supplemental information can be found online at https://doi.org/10.1016/j.xcrm.2022.100765.

## ACKNOWLEDGMENTS

The authors acknowledge financial support by the National Natural Science Foundation of China (62175190), the Foundation Research Fund of Shenzhen Science and Technology Program (JCYJ20190808154409678), and Key technology development and application of novel coronavirus detection in cold chain food and related environment (2021ACB002).

## AUTHOR CONTRIBUTIONS

Conceptualization and design, L.C. and Y.Y.; performing experiments, L.C., Y.L., and L.Y.; chip fabrication, J.Z., P.T., F.W., and K.Y.; system construction, L.C., L.Y., H.X., and Y.L.; methodology, L.C., L.Y., Y.L., L.M., F.W., L.B., H.X., F.Z., Y.C., and Y.Z.; investigation, L.C.,L.Y., Y.L., and Y.Y.; visualization, L.C. and P.T.; writing – original draft, L.C., L.Y., and Y.L.; writing – review and editing, L.C., Y.L., L.Y., Y.Y., and Y.Z.; Y.Y. supervised and coordinated all of the work.

## DECLARATION OF INTERESTS

The authors declare that they have no conflict of interest.

Received: May 15, 2022
Revised: July 26, 2022
Accepted: September 14, 2022
Published: October 6, 2022

## REFERENCES

1. Abuelkasem, E., Lu, S., Tanaka, K., Planinsic, R., and Sakai, T. (2016). Comparison between thrombelastography and thromboelastometry in hyperfibrinolysis detection during adult liver transplantation. Br. J. Anaesth. *116*, 507–512. https://doi.org/10.1093/bja/aew023.
2. Min, J., Chin, L.K., Oh, J., Landeros, C., Vinegoni, C., Lee, J., Lee, S.J., Park, J.Y., Liu, A.-Q., Castro, C.M., et al. (2020). CytoPAN-Portable cellular analyses for rapid point-of-care cancer diagnosis. Sci. Transl. Med. *12*, eaaz9746. https://doi.org/10.1126/scitranslmed.aaz9746.
3. Wikkelsø, A., Wetterslev, J., Møller, A.M., and Afshari, A. (2017). Thromboelastography (TEG) or rotational thromboelastometry (ROTEM) to monitor haemostatic treatment in bleeding patients: a systematic review with meta-analysis and trial sequential analysis. Anaesthesia *72*, 519–531. https://doi.org/10.1111/anae.13765.
4. O'Leary, J.G., Greenberg, C.S., Patton, H.M., and Caldwell, S.H. (2019). AGA clinical practice update: coagulation in cirrhosis. Gastroenterology *157*, 34–43.e1. https://doi.org/10.1053/j.gastro.2019.03.070.
5. De Pietri, L., Bianchini, M., Montalti, R., De Maria, N., Di Maira, T., Begliomini, B., Gerunda, G.E., Di Benedetto, F., Garcia-Tsao, G., and Villa, E. (2016). Thrombelastography-guided blood product use before invasive procedures in cirrhosis with severe coagulopathy: a randomized,


B

| | Optofluidic imaging analyser |
|---|---|
| Device properties: | 8 cm × 6 cm × 3.5 cm<br>Weigh: < 0.7 kg<br>**Smart diagnosis** |
| Blood sample volume: | < 10 μL<br>Minimally invasive |
| Application Scenarios: | Hospitals; Community medical centers; Point-of-care; Home, etc.<br>Portable and easy to operate |

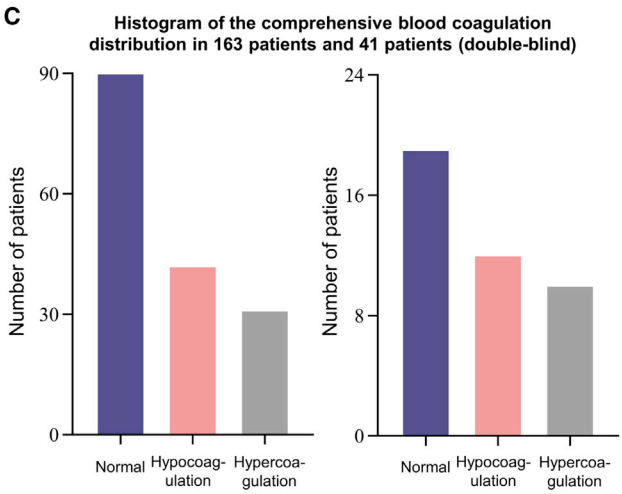


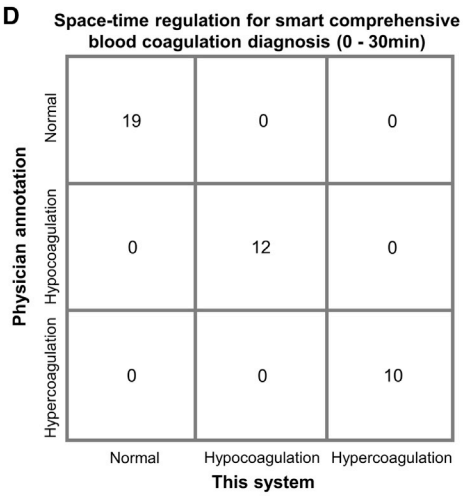


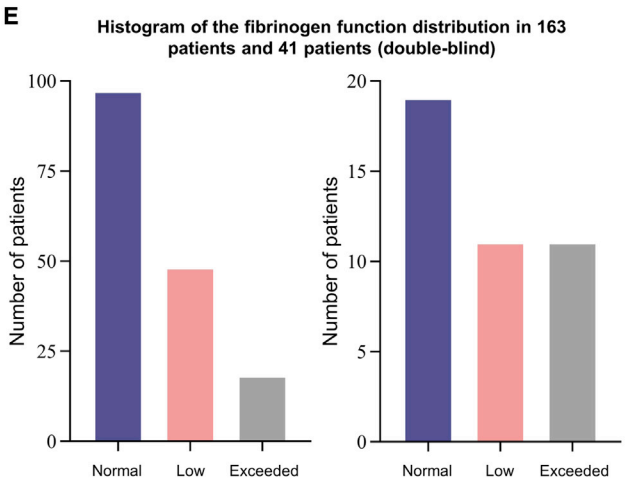


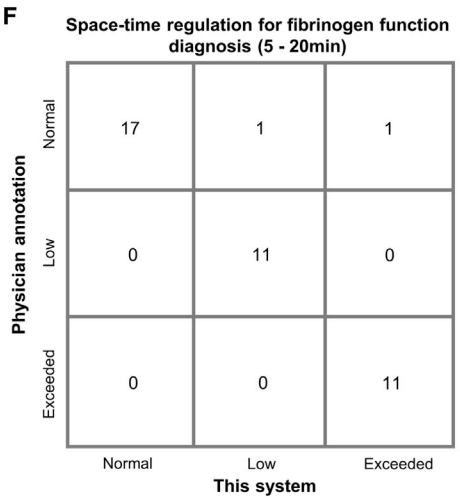


**Figure 6. The clinical assays of smart comprehensive coagulation and fibrinogen function diagnoses using this system**

(A) The photo of the smart space-time-regulated optofluidic imaging analyzer.

(B) The detailed parameters of the optofluidic imaging analyzer.

(C) Histogram of the comprehensive blood coagulation distribution in 163 patients and 41 patients (double-blind test).

*(legend continued on next page)*

controlled trial. Hepatology *63*, 566–573. https://doi.org/10.1002/hep.28148.

6. Whiting, D., and DiNardo, J.A. (2014). TEG and ROTEM: technology and clinical applications. Am. J. Hematol. *89*, 228–232. https://doi.org/10.1002/ajh.23599.
7. Bolliger, D., Seeberger, M.D., and Tanaka, K.A. (2012). Principles and practice of thromboelastography in clinical coagulation management and transfusion practice. Transfus. Med. Rev. *26*, 1–13. https://doi.org/10.1016/j.tmrv.2011.07.005.
8. Yang, K., Wu, J., Santos, S., Liu, Y., Zhu, L., and Lin, F. (2019). Recent development of portable imaging platforms for cell-based assays. Biosens. Bioelectron. *124-125*, 150–160. https://doi.org/10.1016/j.bios.2018.10.024.
9. Chen, L., Liu, Y., Xu, H., Ma, L., Wang, Y., Yu, L., Wang, F., Zhu, J., Hu, X., Yi, K., et al. (2021). Touchable cell biophysics property recognition platforms enable multifunctional blood smart health care. Microsyst. Nanoeng. *7*, 103. https://doi.org/10.1038/s41378-021-00329-z.
10. Shi, Y., Liu, H.L., Zhu, X.Q., Zhu, J.M., Zuo, Y.F., Yang, Y., Jiang, F.H., Sun, C.J., Zhao, W.H., and Han, X.T. (2018). Optofluidic differential colorimetry for rapid nitrite determination. Lab Chip *18*, 2994–3002. https://doi.org/10.1039/c8lc00690c.
11. Zhu, H.H., Zou, J., Zhang, H., Shi, Y.Z., Luo, S.B., Wang, N., Cai, H., Wan, L.X., Wang, B., Jiang, X.D., et al. (2022). Space-efficient optical computing with an integrated chip diffractive neural network. Nat. Commun. *13*, 1044. https://doi.org/10.1038/s41467-022-28702-0.
12. Weissleder, R., and Lee, H. (2020). Automated molecular-image cytometry and analysis in modern oncology. Nat. Rev. Mater. *5*, 409–422. https://doi.org/10.1038/s41578-020-0180-6.
13. Shi, Y., Zhao, H., Chin, L.K., Zhang, Y., Yap, P.H., Ser, W., Qiu, C.W., and Liu, A.Q. (2020). Optical potential-well Array for high-selectivity, massive trapping and sorting at nanoscale. Nano Lett. *20*, 5193–5200. https://doi.org/10.1021/acs.nanolett.0c01464.
14. Yang, X., Luo, Y., Liu, Y., Gong, C., Wang, Y., Rao, Y.-J., Peng, G.-D., and Gong, Y. (2020). Mass production of thin-walled hollow optical fibers enables disposable optofluidic laser immunosensors. Lab Chip *20*, 923–930. https://doi.org/10.1039/c9lc01216h.
15. Zhang, H., Thompson, J., Gu, M., Jiang, X.D., Cai, H., Liu, P.Y., Shi, Y., Zhang, Y., Karim, M.F., Lo, G.Q., et al. (2021). Efficient on-chip training of optical neural networks using genetic algorithm. ACS Photonics *8*, 1662–1672. https://doi.org/10.1021/acsphotonics.1c00035.
16. Tan, X., Broses, L.J., Zhou, M., Day, K.C., Liu, W., Li, Z., Weizer, A.Z., Munson, K.A., Khaing Oo, M.K., Day, M.L., and Fan, X. (2020). Multiparameter urine analysis for quantitative bladder cancer surveillance of orthotopic xenografted mice. Lab Chip *20*, 634–646. https://doi.org/10.1039/c9lc01006h.
17. Fan, X., and White, I.M. (2011). Optofluidic microsystems for chemical and biological analysis. Nat. Photonics *5*, 591–597. https://doi.org/10.1038/nphoton.2011.206.
18. Chen, L., Zheng, Y., Liu, Y., Tian, P., Yu, L., Bai, L., Zhou, F., Yang, Y., Cheng, Y., Wang, F., et al. (2022). Microfluidic-based in vitro thrombosis model for studying microplastics toxicity. Lab Chip *22*, 1344–1353. https://doi.org/10.1039/d1lc00989c.
19. Luo, S., Shi, Y., Chin, L.K., Hutchinson, P.E., Zhang, Y., Chierchia, G., Talbot, H., Jiang, X., Bourouina, T., and Liu, A.-Q. (2021). Machine-learning-assisted intelligent imaging flow cytometry: a review. Adv. Intell. Syst. *3*, 2100073. https://doi.org/10.1002/aisy.202100073.
20. Louka, M., and Kaliviotis, E. (2021). Development of an optical method for the evaluation of whole blood coagulation. Biosensors *11*, 113. https://doi.org/10.3390/bios11040113.
21. Chen, Q., Tong, X., Zhu, Y., Tsoi, C.C., Jia, Y., Li, Z., and Zhang, X. (2020). Aberration-free aspherical in-plane tunable liquid lenses by regulating local curvatures. Lab Chip *20*, 995–1001. https://doi.org/10.1039/c9lc01217f.
22. Yao, Z., Kwan, C.C., and Poon, A.W. (2020). An optofluidic "tweeze-and-drag" cell stretcher in a microfluidic channel. Lab Chip *20*, 601–613. https://doi.org/10.1039/c9lc01026b.
23. Li, Z., Zhang, H., Nguyen, B.T.T., Luo, S., Liu, P.Y., Zou, J., Shi, Y., Cai, H., Yang, Z., Jin, Y., et al. (2021). Smart ring resonator-based sensor for multi-component chemical analysis via machine learning. Photon. Res. *9*, B38–B44. https://doi.org/10.1364/prj.411825.
24. Zhu, J., Zhu, X., Zuo, Y., Hu, X., Shi, Y., Liang, L., and Yang, Y. (2019). Optofluidics: the interaction between light and flowing liquids in integrated devices. Opto-Electron. Adv *2*, 19000701–19000710. https://doi.org/10.29026/oea.2019.190007.
25. Jin, N.Z., and Gopinath, S.C.B. (2016). Potential blood clotting factors and anticoagulants. Biomed. Pharmacother. *84*, 356–365. https://doi.org/10.1016/j.biopha.2016.09.057.
26. McFadyen, J.D., and Kaplan, Z.S. (2015). Platelets are not just for clots. Transfus. Med. Rev. *29*, 110–119. https://doi.org/10.1016/j.tmrv.2014.11.006.
27. Sikora, J., Karczmarska-Wódzka, A., Bugieda, J., and Sobczak, P. (2021). The use of total thrombus formation analysis system as a tool to assess platelet function in bleeding and thrombosis risk-A systematic review. Int. J. Mol. Sci. *22*, 8605. https://doi.org/10.3390/ijms22168605.
28. Hesamian, M.H., Jia, W., He, X., and Kennedy, P. (2019). Deep learning techniques for medical image segmentation: achievements and challenges. J. Digit. Imag. *32*, 582–596. https://doi.org/10.1007/s10278-019-00227-x.
29. Lakhani, P., Gray, D.L., Pett, C.R., Nagy, P., and Shih, G. (2018). Hello world deep learning in medical imaging. J. Digit. Imag. *31*, 283–289. https://doi.org/10.1007/s10278-018-0079-6.
30. Zhu, J., Han, G., Hu, X., Zuo, Y., Chen, L., Wang, F., Yang, Y., Jiang, F., Sun, C., Zhao, W., and Han, X. (2020). A portable and accurate phosphate sensor using a gradient fabry-perot array. ACS Sens. *5*, 1381–1388. https://doi.org/10.1021/acssensors.0c00090.
31. Wang, F., Zhu, J., Hu, X., Chen, L., Zuo, Y., Yang, Y., Jiang, F., Sun, C., Zhao, W., and Han, X. (2021). Rapid nitrate determination with a portable lab-on-chip device based on double microstructured assisted reactors. Lab Chip *21*, 1109–1117. https://doi.org/10.1039/d0lc01057j.
32. Zhu, J.M., Shi, Y., Zhu, X.Q., Yang, Y., Jiang, F.H., Sun, C.J., Zhao, W.H., and Han, X.T. (2017). Optofluidic marine phosphate detection with enhanced absorption using a Fabry-Perot resonator. Lab Chip *17*, 4025–4030. https://doi.org/10.1039/c7lc01016h.
33. Wang, Y., Zhang, Y., Navarro, L., Eker, O.F., Corredor Jerez, R.A., Chen, Y., Zhu, Y., and Courbebaisse, G. (2016). Multilevel segmentation of intracranial aneurysms in CT angiography images. Med. Phys. *43*, 1777–1786. https://doi.org/10.1118/1.4943375.
34. Olabarriaga, S.D., Rouet, J.M., Fradkin, M., Breeuwer, M., and Niessen, W.J. (2005). Segmentation of thrombus in abdominal aortic aneurysms from CTA with nonparametric statistical grey level appearance modeling. IEEE Trans. Med. Imag. *24*, 477–485. https://doi.org/10.1109/tmi.2004.843260.

(D) Confusion matrices comparing the performance on 41 double-blind clinical patients' comprehensive blood coagulation diagnosis between physician annotation and this system.

(E) Histogram of the fibrinogen function distribution in 161 patients and 41 patients (double-blind test).

(F) Confusion matrices comparing the performance on 41 double-blind clinical patients' fibrinogen function diagnosis between physician annotation and this system.

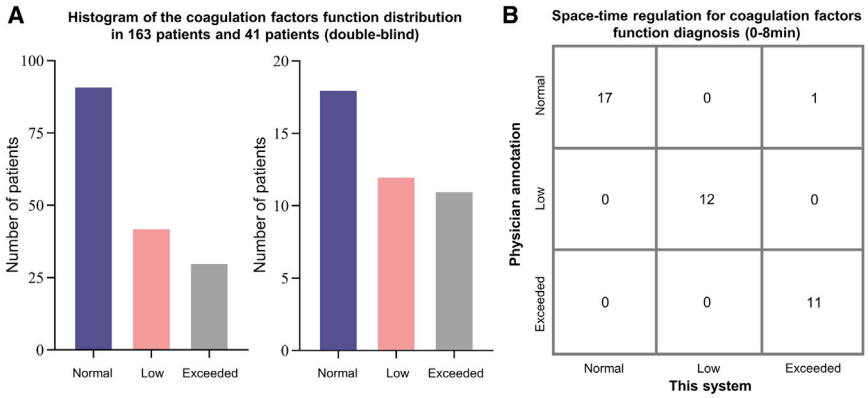


**Figure 7. The clinical assays of smart coagulation factor function diagnoses**

(A) Histogram of the coagulation factor distribution in 161 patients and 41 patients (double-blind test). (B) Confusion matrices comparing the performance on 41 double-blind clinical patients' coagulation factor function diagnosis between physician annotation and this system.

35. Versteeg, H.H., Heemskerk, J.W.M., Levi, M., and Reitsma, P.H. (2013). New fundamentals in hemostasis. Physiol. Rev. *93*, 327–358. https://doi.org/10.1152/physrev.00016.2011.

36. Sakurai, Y., Hardy, E.T., Ahn, B., Tran, R., Fay, M.E., Ciciliano, J.C., Mannino, R.G., Myers, D.R., Qiu, Y., Carden, M.A., et al. (2018). A microengineered vascularized bleeding model that integrates the principal components of hemostasis. Nat. Commun. *9*, 509. https://doi.org/10.1038/s41467-018-02990-x.

37. Jain, A., Barrile, R., van der Meer, A.D., Mammoto, A., Mammoto, T., De Ceunynck, K., Aisiku, O., Otieno, M.A., Louden, C.S., Hamilton, G.A., et al. (2018). Primary human lung alveolus-on-a-chip model of intravascular thrombosis for assessment of therapeutics. Clin. Pharmacol. Ther. *103*, 332–340. https://doi.org/10.1002/cpt.742.

38. Heemskerk, J.W.M., Mattheij, N.J.A., and Cosemans, J.M.E.M. (2013). Platelet-based coagulation: different populations, different functions. J. Thromb. Haemostasis *11*, 2–16. https://doi.org/10.1111/jth.12045.

39. Yang, H., Kim, A., David, T., Palmer, D., Jin, T., Tien, J., Huang, F., Cheng, T., Coughlin, S.R., Jan, Y.N., and Jan, L.Y. (2012). TMEM16F forms a $Ca^{2+}$ activated cation channel required for lipid scrambling in platelets during blood coagulation. Cell *151*, 111–122. https://doi.org/10.1016/j.cell.2012.07.036.

40. Koo, H.J., Lim, S., Choe, J., Choi, S.-H., Sung, H., and Do, K.-H. (2018). Radiographic and CT features of viral pneumonia. Radiographics *38*, 719–739. https://doi.org/10.1148/rg.2018170048.

41. Wong, V.W.-S., Adams, L.A., de Lédinghen, V., Wong, G.L.-H., and Sookoian, S. (2018). Noninvasive biomarkers in NAFLD and NASH - current progress and future promise. Nat. Rev. Gastroenterol. Hepatol. *15*, 461–478. https://doi.org/10.1038/s41575-018-0014-9.

42. Guzman-Sepulveda, J.R., Argueta-Morales, R., DeCampli, W.M., and Dogariu, A. (2017). Real-time intraoperative monitoring of blood coagulability via coherence-gated light scattering. Nat. Biomed. Eng. *1*, 0028. https://doi.org/10.1038/s41551-017-0028.

43. Kuprash, A.D., Shibeko, A.M., Vijay, R., Nair, S.C., Srivastava, A., Ataullakhanov, F.I., Panteleev, M.A., and Balandina, A.N. (2018). Sensitivity and robustness of spatially dependent thrombin generation and fibrin clot propagation. Biophys. J. *115*, 2461–2473. https://doi.org/10.1016/j.bpj.2018.11.009.

44. Mohammadi Aria, M., Erten, A., and Yalcin, O. (2019). Technology advancements in blood coagulation measurements for point-of-care diagnostic testing. Front. Bioeng. Biotechnol. *7*, 395. https://doi.org/10.3389/fbioe.2019.00395.

45. Roullet, S., Labrouche, S., Chiche, L., Nouette-Gaulain, K., Laurent, C., and Freyburger, G. (2019). The Thrombodynamics (R) analyzer: a new thrombin generation analyzer compared to the Calibrated Automated Thrombogram (R) in liver transplantation. Thromb. Res. *175*, 37–39. https://doi.org/10.1016/j.thromres.2019.01.015.

46. Chan, J., Michaelsen, K., Estergreen, J.K., Sabath, D.E., and Gollakota, S. (2022). Micro-mechanical blood clot testing using smartphones. Nat. Commun. *13*, 831. https://doi.org/10.1038/s41467-022-28499-y.

47. Shaydakov, M.E., Sigmon, D.F., and Blebea, J. (2022). Thromboelastography. In StatPearls (StatPearls Publishing). https://www.ncbi.nlm.nih.gov/books/NBK537061/.

48. Shi, Y.Z., Xiong, S., Zhang, Y., Chin, L.K., Chen, Y.Y., Zhang, J.B., Zhang, T.H., Ser, W., Larrson, A., Lim, S.H., et al. (2018). Sculpting nanoparticle dynamics for single-bacteria-level screening and direct binding-efficiency measurement. Nat. Commun. *9*, 815. https://doi.org/10.1038/s41467-018-03156-5.

49. Shi, Y., Xiong, S., Chin, L.K., Zhang, J., Ser, W., Wu, J., Chen, T., Yang, Z., Hao, Y., Liedberg, B., et al. (2018). Nanometer-precision linear sorting with synchronized optofluidic dual barriers. Sci. Adv. *4*, eaao0773. https://doi.org/10.1126/sciadv. aao0773.

50. Im, H., Pathania, D., McFarland, P.J., Sohani, A.R., Degani, I., Allen, M., Coble, B., Kilcoyne, A., Hong, S., Rohrer, L., et al. (2018). Design and clinical validation of a point-of-care device for the diagnosis of lymphoma via contrast-enhanced microholography and machine learning. Nat. Biomed. Eng. *2*, 666–674. https://doi.org/10.1038/s41551-018-0265-3.

51. Qi, L., Zhang, X., Dou, W., Hu, C., Yang, C., and Chen, J. (2018). A two-stage locality-sensitive hashing based approach for privacy-preserving mobile service recommendation in cross-platform edge environment. Future Generat. Comput. Syst. *88*, 636–643. https://doi.org/10.1016/j.future.2018.02.050.

52. Hossain, M.S., and Muhammad, G. (2018). Environment classification for Irban big data using deep learning. IEEE Commun. Mag. *56*, 44–50. https://doi.org/10.1109/mcom.2018.1700577.

53. Windberger, U., Dibiasi, C., Lotz, E.M., Scharbert, G., Reinbacher-Koestinger, A., Ivanov, I., Ploszczanski, L., Antonova, N., and Lichtenegger, H. (2020). The effect of hematocrit, fibrinogen concentration and temperature on the kinetics of clot formation of whole blood. Clin. Hemorheol. Microcirc. *75*, 431–445. https://doi.org/10.3233/ch-190799.

54. Whelihan, M.F., Kiankhooy, A., and Brummel-Ziedins, K.E. (2014). Thrombin generation and fibrin clot formation under hypothermic conditions: an in vitro evaluation of tissue factor initiated whole blood coagulation. J. Crit. Care *29*, 24–30. https://doi.org/10.1016/j.jcrc.2013.10.010.

## STAR★METHODS

### KEY RESOURCES TABLE

| REAGENT or RESOURCE | SOURCE | IDENTIFIER |
|---|---|---|
| Chemicals, peptides, and recombinant proteins | | |
| Calcium chloride solution | Sigma-Aldrich | Cas# 10043-52-4 |
| PE anti-human CD41 Antibody | BioLegend | Cat# 303706; RRID:AB_314376 |
| Alexa Fluor™ 488 fibrinogen | Thermo Fisher | Cat# F13191 |
| Critical commercial assays | | |
| Standard clinical Thromboelastography test | Zhongnan Hospital of Wuhan University, Wuhan, China | N/A |
| Deposited data | | |
| Deep learning models for coagulation function diagnoses | This paper | Figshare Data: https://doi.org/10.6084/m9.figshare.21206081 |
| The 163 volunteered clinical patients' pathology report (deep learning model development) | This paper | Table S1; Table S2 |
| The 41 volunteered clinical patients' pathology report (clinical assays) | This paper | |
| Software and algorithms | | |
| Python | Python Software Foundation | V3.6.1 |
| GraphPad Prism | GraphPad | https://www.graphpad.com/ |
| ImageJ | NIH | https://imagej.nih.gov/ij/ |
| Solid works | Dassault Systemes | https://www.solidworks.com/zh-hans |
| MATLAB | MathWorks | https://ww2.mathworks.cn/products/matlab.html |
| Android Studio | Google | https://developer.android.google.cn/studio/ |
| 3D Studio Max | Autodesk | https://www.autodesk.com.cn/ |
| Other | | |
| Lithography and chip preparation | Key Laboratory of Artificial Micro- and Nano-Structures of Ministry of Education, School of Physics & technology, Wuhan University | N/A |
| Equipment design and 3D printing | Key Laboratory of Artificial Micro- and Nano-Structures of Ministry of Education, School of Physics & technology, Wuhan University | N/A |

### RESOURCE AVAILABILITY

#### Lead contact

Requests for further information and reagents may be addressed to the corresponding author: Yi Yang (yangyiys@whu.edu.cn).

#### Materials availability

This study did not generate new unique reagents.

#### Data and code availability

- The confidential medical records data reported in this study cannot be deposited in a public repository. To request access, contact the Lead Author. In addition, pathological distribution from these patients have been found at Figshare Data: https://doi.org/10.6084/m9.figshare.21113839.
- The origin code of developed models has been included at Figshare Data: https://doi.org/10.6084/m9.figshare.21206081 and is publicly available as of the date of publication.

- Any additional information required to reanalyze the data reported in this work paper is available from the lead contact upon request.

## EXPERIMENTAL MODEL AND SUBJECT DETAILS

In this work, the 163 clinical patients were set for space-regulated AI model development for diverse coagulation function diagnoses including coagulation factors, fibrinogen function and comprehensive blood coagulation. And the model was loaded into a developed smartphone/cloud computing system. A double-blind 41 clinical samples test comparison to standard clinical method was used to evaluate clinical performance of this system. The blood samples of clinical patients were collected from the Zhongnan Hospital of Wuhan University. And the volunteers had given informed, written consent. And this project (no. 202265K) has been approved and oversighted by Ethical Approval for Clinical/Scientific Research under Medical Ethics Committee, Zhongnan Hospital of Wuhan University. All experiments were conducted in accordance with the Declaration of Helsinki and the International Ethical Guidelines for Biomedical Research Involving Human Subjects. And detail information of each case is available in Tables S1 and S2.

## METHOD DETAILS

### Fabrication of the optofluidic chip

The microfluidic chips (30 × 14 × 3 mm) were fabricated using a standard soft lithography process. The chip structure was etched onto a silicon wafer covered with a uniform photoresist SU-8 via the mask plate (Beijing Machinery Industry Automation Research Institute Co., Beijing, China), and the reusable master plate was created on the silicon template to manufacture the microfluidic chips. The 20 g of polydimethylsiloxane (PDMS) prepolymer (Dow Corning, Sylgard 184) was poured over the silicon template (5 inches) and stored in an oven at 75°C for 1 h. The PDMS replica was stripped from the master plate and sealed to a flat slide surface after plasma oxidation bonding. The microfluidic chip includes an inlet, an outlet, a symmetrical microfluidic channel and a circular chamber. The width and height of the symmetrical microfluidic channel are 100 and 60 μm. The size of the whole microfluidic chamber is 24 mm × 10 mm×60 μm, respectively.

### Design of the portable imaging system

As suggested by senior physicians, the device is split designed to prevent clinical cross-infection. The 3D printed shell (80 × 60 × 35 mm) was fabricated by ZRapid iSLA660 with acrylonitrile butadiene styrene (C-UV 9400E), which includes two parts (upper and lower layer). The lower layer is used to set the developed optical imaging system[9] (resolution: 1 μm, H × V: 1.81 × 1.02 mm, working distance: 0.75 mm, Figure S1), which includes camera module (CMOS IMX214, RERVISION), optics lens (KENWEIJIESI), USB module and LED module (C5050, BDQ), and the upper layer is used for optofluidic chip insertion. The size of chip insertion window is 50 mm (length) × 5 mm (width). The calibration operation is used for autofocus or manual focus and it keep the focal plane stable for subsequent measurements. To make the device as lightweight and portable as possible, the imaging module is not equipped with a power supply system inside and we use a USB module to power and transfer data.

### Image differential computing process for clotting biophysical properties acquisition

In this work, the differential computing refers to the use of pixel differences between consecutive image frames to detect the coagulation process. Through the portable optical imaging system, the smartphone collected the continuous fields of view of the blood clotting, and the interval time was 20s. The images were converted into grayscale images by the channel splitting and the formula for grayscale processing of color images is $Y(x,y) = (1 * R(x,y) + 0 * G(x,y) + 0 * B(x,y))$, where $R(x,y)$, $G(x,y)$ and $B(x,y)$ are RGB color components of Point $(x,y)$. The differential method follows the formula:

$$d_n(x, y) = \begin{cases} f_n(x, y) - f_{n-1}(x, y), f_n(x,y) - f_{n-1}(x, y) \leq 0 \\ 0, f_n(x, y) - f_{n-1}(x, y) > 0 \end{cases}$$

where $f_n(x,y)$ is the current frame, $f_{n-1}(x,y)$ is the previous frame. $d_n(x,y)$ is the image after differential computing. In order to calculate the blood clotting area and the average gray value, the grayscale value of the pixel points for each image are first summed up. The blood clotting area is the sum of the extracted pixel points, and the average gray value is the quotient of the total gray value and the blood clotting area, i.e.mean = sum/area, 'mean' refers to the optical average gray value, 'sum' refers to the total gray value, and 'area' refers to the clotting area. Finally, the image differential computing processed data was loaded into the input vector table.[9,10,51,52]

### Developed deep learning system

The 163 clinical cases were set for space time-based neural network (convolutional neural networks) diagnostic model development. The OCB properties with differentially computing process were inputted as vector tables for model development (Figures S4 and S5), the 5-min interval differential computation has 12 input vectors, the 3-min interval differential computation has 20 input vectors, the 1-min interval differential computation has 60 input vectors and the 20-s interval differential computation has 180 input vectors. The

trained neural network contained six convolutions and three fully connected layers, the 3 fully connected layers contained 180 (the 20-s interval differential), 64, and 20 vectors. The dropout method was used in the training process to avoid overfitting and increase generalization performance. The training set accounts for 70%, and the test set accounts for 30%.[8,9,19,23] The 70% of the data is randomly selected as the training set each time and the remaining 30% is retained as the validation set during clinical sample training process. The training process performs iterations of twenty large cycles. And the algorithm can be fully extended to an inexpensive Raspberry Pi module for low-resourced environments.

### Image acquisition interval selection

As shown in Figure S6, the AI models for comprehensive coagulation diagnosis (0–30 min) with gradient image acquisition intervals (20 s, 1 min, 3 min, 5 min) were performed, and the results show that the deep learning model based on 5-min interval differential computation has a comprehensive test accuracy of 83.2% (94.7% diagnosing accuracy of health, 71.6% diagnosing accuracy of hypocoagulation, 63% diagnosing accuracy of hypercoagulation), the deep learning model based on 3-min interval differential computation has a comprehensive test accuracy of 88.3% (93.1% diagnosing accuracy of health, 81.7% diagnosing accuracy of hypocoagulation, 82.5% diagnosing accuracy of hypercoagulation), the deep learning model based on 1-min interval differential computation has a comprehensive test accuracy of 94.8% (93.8% diagnosing accuracy of health, 93.3% diagnosing accuracy of hypocoagulation, 100.0% diagnosing accuracy of hypercoagulation) and the deep learning model based on 20-s interval differential computation has a comprehensive test accuracy of 98.6% (98.7% diagnosing accuracy of health, 98.3% diagnosing accuracy of hypocoagulation, 98.8% diagnosing accuracy of hypercoagulation). These results suggest that the deep learning model has better diagnostic accuracy with shorter image acquisition interval, and it's because of that the ORBC properties acquisition are more detailed with shorter image acquisition interval. While the image acquisition interval is further shortened, it will increase the requirements of edge computing based smartphone for images storage and computation.[9,30–32,51,52] Therefore, the 20-s image acquisition interval was selected due to the balanced accuracy and storage need.

### Fluorescence characterization of clotting

The 100 μL of blood sample was incubated with 5 μL 0.2 mg/mL PE anti-human CD41 Antibody (sigma) and 0.13 μL 2 μg/mL Alexa Fluor™ 488 fibrinogen (Thermo Fisher) in the dark at room temperature for 15 min. The fluorescent images of blood clotting (room temperature: 26°C)[20,53,54] were captured via a confocal microscope (Nikon, A1R).

### Blood assays

To accurately assess the performance of the method, both this system and the TEG instrument use the same blood sample and standard preparing procedures (Kaolin-activated and $Ca^{2+}$-activated) to avoid biased results due to time sensitivity, in this work, the $Ca^{2+}$ reagent used are scaled down in proportion to the amount of TEG blood (340:10) before injection.

### Comparison of third-party TEG instrument test

The clinical TEG instrument performs test preparing with the following process: The normal cup was placed in the cup holder and 20 μL of calcium chloride solution was added in the cup; 1 mL of blood sample was added to the Kaolin activator tube and then 340 μL of Kaolin-activated blood sample was added to the cup. The TEG instrument then performs the test on the physics basis of monitoring the amplitude changes of a high-precision probe, and a senior physician performs the diagnosis based the recorded curve and parameters. The third-party TEG instrument test of 41 clinical patients was performed jointly using two senior laboratory physicians of Zhongnan hospital.

## QUANTIFICATION AND STATISTICAL ANALYSIS

All statistical tests were performed using GraphPad Prism version 8.